RP-CARS: label-free optical readout of the myelin intrinsic healthiness

Giuseppe de Vito,[1,2,*] Ilaria Tonazzini,[3] Marco Cecchini,[3] and Vincenzo Piazza[1]

[1]Center for Nanotechnology Innovation @NEST, Istituto Italiano di Tecnologia, Piazza San Silvestro 12, I-56127 Pisa, Italy
[2]NEST, Scuola Normale Superiore, Piazza San Silvestro 12, I-56127 Pisa, Italy
[3]NEST, Scuola Normale Superiore and Istituto Nanoscienze-CNR, Piazza San Silvestro 12, Pisa 56127, Italy
*giuseppe.devito@iit.it

Abstract: Here we present a method based on Rotating-Polarization Coherent Anti-Stokes Raman Scattering (RP-CARS) imaging to assess the myelin health status in mouse sciatic nerves. Differently from the existing techniques, our method is based on the readout of intrinsic molecular architecture rather than on the image analysis, relying on the fact that healthy myelin is characterized by a high degree of molecular order. We exploit RP-CARS imaging to demonstrate that the degree of spatial anisotropy of the CARS signal displays a strong correlation with the g-ratio (a well-known image-based index of myelin damage) in a chemical-damage model and therefore that the former is a good indicator for the local myelin health status.

©2014 Optical Society of America

OCIS codes: (300.6230) Spectroscopy, coherent anti-Stokes Raman scattering; (180.4315) Nonlinear microscopy; (170.1420) Biology; (170.3880) Medical and biological imaging; (170.4730) Optical pathology; (170.6935) Tissue characterization.

References and links

1. E. Rusell, Martenson, *Myelin: Biology and Chemistry* (CRC, 1992).
2. C. L. Evans, E. O. Potma, M. Puoris'haag, D. Côté, C. P. Lin, and X. S. Xie, "Chemical imaging of tissue in vivo with video-rate coherent anti-Stokes Raman scattering microscopy," Proc. Natl. Acad. Sci. U.S.A. **102**(46), 16807–16812 (2005).
3. E. Bélanger, J. Crépeau, S. Laffray, R. Vallée, Y. De Koninck, and D. Côté, "Live animal myelin histomorphometry of the spinal cord with video-rate multimodal nonlinear microendoscopy," J. Biomed. Opt. **17**(2), 021107 (2012).
4. P. Maker and R. Terhune, "Study of optical effects due to an induced polarization third order in the electric field strength," Phys. Rev. **137**(3A), A801–A818 (1965).
5. Y. Fu, T. B. Huff, H. W. Wang, H. Wang, and J. X. Cheng, "Ex vivo and in vivo imaging of myelin fibers in mouse brain by coherent anti-Stokes Raman scattering microscopy," Opt. Express **16**(24), 19396–19409 (2008).
6. Y. Fu, W. Sun, Y. Shi, R. Shi, and J. X. Cheng, "Glutamate excitotoxicity inflicts paranodal myelin splitting and retraction," PLoS ONE **4**(8), e6705 (2009).
7. Y. Fu, H. Wang, T. B. Huff, R. Shi, and J. X. Cheng, "Coherent anti-stokes Raman scattering imaging of myelin degradation reveals a calcium-dependent pathway in lyso-PtdCho-induced demyelination," J. Neurosci. Res. **85**(13), 2870–2881 (2007).
8. H. Ouyang, W. Sun, Y. Fu, J. Li, J. X. Cheng, E. Nauman, and R. Shi, "Compression induces acute demyelination and potassium channel exposure in spinal cord," J. Neurotrauma **27**(6), 1109–1120 (2010).
9. T. B. Huff, Y. Shi, W. Sun, W. Wu, R. Shi, and J. X. Cheng, "Real-time CARS imaging reveals a calpain-dependent pathway for paranodal myelin retraction during high-frequency stimulation," PLoS ONE **6**(3), e17176 (2011).
10. Y. Fu, T. J. Frederick, T. B. Huff, G. E. Goings, S. D. Miller, and J. X. Cheng, "Paranodal myelin retraction in relapsing experimental autoimmune encephalomyelitis visualized by coherent anti-Stokes Raman scattering microscopy," J. Biomed. Opt. **16**(10), 106006 (2011).
11. J. Imitola, D. Côté, S. Rasmussen, X. S. Xie, Y. Liu, T. Chitnis, R. L. Sidman, C. P. Lin, and S. J. Khoury, "Multimodal coherent anti-Stokes Raman scattering microscopy reveals microglia-associated myelin and axonal dysfunction in multiple sclerosis-like lesions in mice," J. Biomed. Opt. **16**(2), 021109 (2011).
12. Y. Shi, D. Zhang, T. B. Huff, X. Wang, R. Shi, X. M. Xu, and J. X. Cheng, "Longitudinal in vivo coherent anti-Stokes Raman scattering imaging of demyelination and remyelination in injured spinal cord," J. Biomed. Opt. **16**(10), 106012 (2011).

13. Y. Fu, T. M. Talavage, and J. X. Cheng, "New imaging techniques in the diagnosis of multiple sclerosis," Expert Opin Med Diagn **2**(9), 1055–1065 (2008).
14. T. Meyer, M. Chemnitz, M. Baumgartl, T. Gottschall, T. Pascher, C. Matthäus, B. F. M. Romeike, B. R. Brehm, J. Limpert, A. Tünnermann, M. Schmitt, B. Dietzek, and J. Popp, "Expanding multimodal microscopy by high spectral resolution coherent anti-Stokes Raman scattering imaging for clinical disease diagnostics," Anal. Chem. **85**(14), 6703–6715 (2013).
15. S. Bégin, E. Bélanger, S. Laffray, B. Aubé, É. Chamma, J. Bélisle, S. Lacroix, Y. De Koninck, and D. Côté, "Local assessment of myelin health in a multiple sclerosis mouse model using a 2D Fourier transform approach," Biomed. Opt. Express **4**(10), 2003–2014 (2013).
16. G. de Vito, A. Bifone, and V. Piazza, "Rotating-polarization CARS microscopy: combining chemical and molecular orientation sensitivity," Opt. Express **20**(28), 29369–29377 (2012).
17. H. Wang, Y. Fu, P. Zickmund, R. Shi, and J. X. Cheng, "Coherent anti-stokes Raman scattering imaging of axonal myelin in live spinal tissues," Biophys. J. **89**(1), 581–591 (2005).
18. E. Bélanger, S. Bégin, S. Laffray, Y. De Koninck, R. Vallée, and D. Côté, "Quantitative myelin imaging with coherent anti-Stokes Raman scattering microscopy: alleviating the excitation polarization dependence with circularly polarized laser beams," Opt. Express **17**(21), 18419–18432 (2009).
19. G. de Vito and V. Piazza, "Fast signal analysis in Rotating-Polarization CARS microscopy," Opt. Data Processing and Storage **1**, 1–5 (2014).
20. T. L. Mazely and W. M. Hetherington, "Third-order susceptibility tensors of partially ordered systems," J. Chem. Phys. **87**(4), 1962 (1987).
21. F. Z. Bioud, P. Gasecka, P. Ferrand, H. Rigneault, J. Duboisset, and S. Brasselet, "Structure of molecular packing probed by polarization-resolved nonlinear four-wave mixing and coherent anti-Stokes Raman-scattering microscopy," Phys. Rev. A **89**(1), 013836 (2014).
22. S. M. Hall and N. A. Gregson, "The in vivo and ultrastructural effects of injection of lysophosphatidyl choline into myelinated peripheral nerve fibres of the adult mouse," J. Cell Sci. **9**(3), 769–789 (1971).
23. T. Coetzee, N. Fujita, J. Dupree, R. Shi, A. Blight, K. Suzuki, K. Suzuki, and B. Popko, "Myelination in the Absence of Galactocerebroside and Sulfatide: Normal Structure with Abnormal Function and Regional Instability," Cell **86**(2), 209–219 (1996).
24. C. O. Hanemann, A. A. W. M. Gabreëls-Festen, and P. De Jonghe, "Axon damage in CMT due to mutation in myelin protein P0," Neuromuscul. Disord. **11**(8), 753–756 (2001).
25. S. P. J. Fancy, S. E. Baranzini, C. Zhao, D. I. Yuk, K. A. Irvine, S. Kaing, N. Sanai, R. J. M. Franklin, and D. H. Rowitch, "Dysregulation of the Wnt pathway inhibits timely myelination and remyelination in the mammalian CNS," Genes Dev. **23**(13), 1571–1585 (2009).
26. F. Munhoz, H. Rigneault, and S. Brasselet, "Polarization-resolved four-wave mixing microscopy for structural imaging in thick tissues," J. Opt. Soc. Am. B **29**(6), 1541–1550 (2012).

1. Introduction

Myelin is a biological structure present in all the gnathostomata [1] that consists in a thin insulating layer wrapped around a subgroup of axons. It increases the transverse resistance and reduces the capacitance making it possible the saltatory conduction of action potentials and therefore leads to a critically improved performance of nervous impulse conduction. Myelin pathologies (myelopathies) are frequent diseases that often result in death or inability. Medical treatments exist that have the capacity to slow down the progress of the disease, being able neither to stop it nor to lead to a stable *restitutio ad integrum*. In order to investigate the main causes of myelin damage and its temporal progression many techniques are currently employed, such as histochemistry, electron microscopy, immunofluorescence, and magnetic resonance imaging (MRI). However, the first two require complex sample preparation and for this reason they are unsuitable for live imaging. The third, immunofluorescence, as well as its derivatives, confocal and two-photon imaging, relies on the use of fluorescent probes to generate the image contrast but fluorophores and the associated sample processing (i.e. fixation for immunostaining) might modify the biological properties of the target molecule and can perturb the whole biological process under investigation. MRI, finally, while being capable of in-vivo full-body imaging, lacks of high spatial resolution and contrast specificity. Coherent Anti-Stokes Raman Scattering (CARS), on the other hand, is an innovative imaging modality that permits the study of living specimina [2], also endoscopically in-vivo [3], with excellent chemical contrast and spatial resolution and without the confounding and often tedious use of fluorescent labels.

CARS is a four-wave mixing process in which the frequency difference of a pair of incoming photons ("pump" and "Stokes") matches the vibrational frequency of the molecular

bond of interest. The vibrational mode of the latter is then coherently probed by a third photon that leads to anti-Stokes emission [4]. This approach makes it possible to obtain video-rate, label-free imaging with chemical-selectivity [2]. The strong CARS signal that can be obtained from myelin by targeting the vibrational modes of CH_2 bonds, which are extremely abundant in this structure (comparable only to the adipose tissue), makes this technique a first-choice method to image it and its pathological modification [5].

Indeed, CARS techniques are being increasingly employed and continuously improved to study myelin in basic and clinical research. In basic research, CARS microscopy was employed to elucidate the cellular mechanisms at the basis of the myelin alterations in glutamate excitotoxicity [6], in lysophosphatidylcholine-induced [7] and in compression-induced [8] damage and during high-frequency stimulation [9]. It is also being extensively exploited to study animal models of multiple sclerosis (MS) [10, 11] and remyelination processes [12]. In clinical research, in the recent times, it is being evaluated as a diagnostic tool for MS [13] and for cardiovascular diseases [14]. In particular, due to its characteristics, CARS was proven to be a valuable tool to specifically evaluate the health condition of myelinated fibers. In [7]. this task was accomplished by computing the g-ratio (the ratio between the inner and the outer diameter of the fiber, a well known image-based indicator of myelin healthiness frequently exploited with different imaging techniques) for each fiber in the CARS images. However this approach has some drawbacks, as tracing individual fibers is a very time consuming process and the readout is an average over the circumference of the fiber. To overcome some of these limitations a new method was recently presented to assess the myelin health based on 2D Fourier transform of CARS images [15]. However this method just assesses the presence of directional features in the image and is not based on the intrinsic molecular characteristics. Finally, as the readout is image-wide based, it is not suited to single-fiber studies.

Here, we present a method to assess the myelin health status based on rotating-polarization CARS (RP-CARS) imaging [16], a CARS-based imaging technique that relies on the rotation of the polarization plane of one of the excitation beams and in-phase detection of the generated anti-Stokes Raman signal to determine the local degree of orientation anisotropy of the molecular bonds under investigation and to image their local microscopic orientation. Differently from those mentioned before, our method is based on the readout of intrinsic molecular architecture rather than on image analysis. Our implementation relies on the fact that healthy myelin is characterized by a high degree of molecular order and spatial anisotropy [1] (as depicted in Fig. 1). In particular, owing to the highly symmetrical architecture of acyl chains in myelin, the CARS signal generated by its CH_2 bonds displays strong polarization-orientation dependence [17]. This was initially recognized as an "imaging artifact", leading to an unwanted orientation-dependent contrast, and several methods were proposed to suppress it [5, 18]. However some authors [7] have shown that swollen myelin loses this polarization-orientation dependence, reasonably owing to the fact that the molecular symmetry and spatial anisotropy are also destroyed during (at least some) demyelination processes. This observation suggests that methods able to determine the local molecular order can be successfully exploited to assess the myelin health status.

Here we exploit RP-CARS imaging to demonstrate, in a chemical damage model, that the g-ratio displays a strong correlation with the degree of spatial anisotropy of myelin CH_2 bonds and therefore that the latter is a good indicator of the local myelin health status.
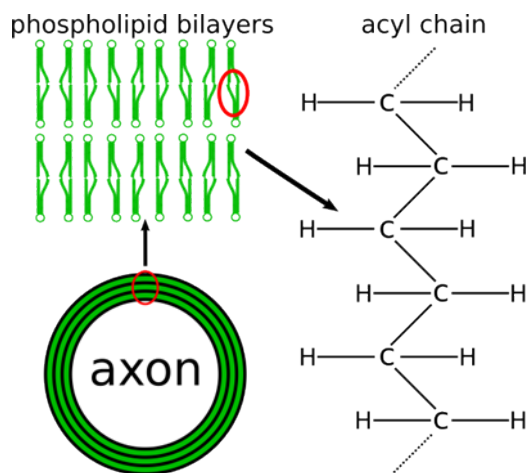
Fig. 1. Myelin structure scheme at increasing magnifications: myelin (in green) is composed of alternated layers of lipids and proteins enrolled around the nerve axon. In the scheme, for the sake of clarity, only the phospholipid moiety is depicted. All the acyl chains of phospholipid bilayers are aligned in radial symmetry. The CH_2 groups that form the acyl chains are, in turn, aligned in an azimuthal symmetry, therefore their average direction is always tangential to the surface of the nerve fiber.

2. Experimental techniques and materials

2.1 The RP-CARS microscope

The RP-CARS setup employed was already described in great details in [16, 19]. Here we summarize it briefly for the sake of clarity: an 806-nm pump-and-probe degenerate beam is created by a Ti-Sa pulsed laser (Coherent Chameleon Vision II). Part of the beam is employed to feed a supercontinuum generator (SCG, photonic-crystal fiber SCG-800 Newport) that generates a broadband Stokes beam. A rotating λ/2 retarder with a compensating λ/4 retarder on the pump-and-probe beam path continuously rotates the polarization of this beam at an angular frequency ω, while a λ/4 retarder on the Stokes beam path transform the latter into a circularly polarized beam. In this way the Stokes beam is circularly polarized, while the pump-and-probe beam features a time-dependent linear polarization.

By using phase-detection techniques [16, 19], we calculate for each image pixel the following three quantities:

- The average over a rotation period of the polarization of the CARS signal, A_{dc}. It is analogous to an artifact-free CARS signal [5, 18].

- The Fourier component at 2ω of the signal, $A_{2\omega}$. It measures of how much the raw CARS signal depends on the polarization orientation of the incident light and, as it will be shown in the following, together with A_{dc}, it allows determining the degree of in-plane anisotropy of the molecular-bond orientation within the point spread function (PSF) volume.

- The phase value ψ that indicates the in-plane average direction of the molecular-bonds.

Before each acquisition session, particular care was taken to adjust the orientation of the two λ/4 retarders in order to compensate for polarization distortions caused by the optics (in particular the dichroic mirrors). Each retarder is rotated both around its optical axis and around the vertical (i.e. perpendicular to the optical table) axis. This procedure is carried out by minimizing the $A_{2\omega}/A_{dc}$ and $A_{4\omega}/A_{dc}$ components of the non-resonant signal originating

from the (isotropic) glass coverslip or WillCo-dish bottom. Values of $A_{2\omega}/A_{dc}$ and $A_{4\omega}/A_{dc}$ as low as 3% can be routinely achieved.

2.2 Biological sample preparation

Adult (aged from P47 to P120) wild type mice (C57BL/6J strain, Jackson Laboratory) were euthanized with cervical dislocation according to the ethical guidelines of the Italian (DL 116/1992) and European Community (86/609/EEC) laws. After death, the sciatic nerves were rapidly surgically explanted and then incubated in constantly oxygenated (95% O_2, 5% CO_2) Krebs-Henseleit Buffer (K3753 Sigma-Aldrich) kept at 38 °C to prevent damages to the fibers.

The explanted nerves were put in WillCo dishes (GWSt-3522, WillCo Wells) and kept immobilized with a custom-made electrophysiology-type anchor.

Lysophosphatidylcholine (L4129 Sigma-Aldrich L-α-Lysophosphatidylcholine from egg yolk, >99%) was first dissolved in 38 °C Krebs-Henseleit Buffer at a concentration of 100 mg/ml and sonicated for 10 minutes. We added the lysophosphatidylcholine solution to the WillCo dish containing the nerves (exposure time: 0-1 h) at the final concentration of 10 mg/ml.

3. Theory

The polarizability involved in a degenerate CARS process is given by:

$$P_i(\omega_3) = \chi_{ijkl}(\omega_3, \omega_1, -\omega_2, \omega_1) E_j(\omega_1) E_k^*(\omega_2) E_l(\omega_1), \qquad (1)$$

where *i, j, k, l* run over the coordinates {*x, y, z*}, ω_1, ω_2, and ω_3 are the angular frequencies of the pump-and-probe beam, of the Stokes beam, and of the emitted CARS radiation respectively, χ_{ijkl} is the third-order susceptibility tensor, and $E_j(\omega)$ the component along the axis *j* of the electric field of one of the incoming photons.

Following [18], the third-order susceptibility of the linear acyl chains of the phospholipidic membranes of the myelin layers can be described with that of a system having cylindrical symmetry with respect to the chain axis (here the *z* axis), which in the case of degenerate four-wave mixing has 21 non-zero terms, with only four of them being independent [20]:

$$\begin{aligned}
c_{11} &= \chi_{xxxx} = \chi_{yyyy}, \\
c_{18} &= \chi_{xxyy} = \chi_{yxyx} = \chi_{yxxy} = \chi_{xyyx} = \chi_{xyxy} = \chi_{yyxx}, \\
c_{16} &= \chi_{xxzz} = \chi_{yyzz} = \chi_{zxzx} = \chi_{zxxz} = \chi_{xzzx} = \chi_{xzxz} = \chi_{zyzy} = \chi_{zyyz} = \chi_{yzzy} \qquad (2) \\
&= \chi_{yzyz} = \chi_{zzxx} = \chi_{zzyy}, \\
c_{33} &= \chi_{zzzz}.
\end{aligned}$$

When the acyl chain is rotated with respect to the laboratory reference systems, the new susceptibility tensor can be calculated as:

$$\chi_{IJKL} = C_{Ii} C_{Jj} C_{Kk} C_{Ll} \chi_{ijkl}, \qquad (3)$$

where uppercase (lowercase) indices refer to the laboratory (molecule) reference system, and C_{Ii} is the direction cosine between axis *I* and *i*, expressed in terms of the *x*-conventional Euler angles φ, ϑ, ψ. It is straightforward to see that a rotation around the *z*-axis – e. g. $\varphi = \pi/4$ – leaves the susceptibility tensor unaltered, as it is expected due to the rotational invariance of the system around the same axis, only if $c_{18} = c_{11}/3$. This leaves only three independent terms in the tensor.

The susceptibility of a "disordered" myelin system, i. e. a system in which the acyl chains are not perfectly aligned along the Z axis, can be calculated integrating the susceptibility tensor over the angular distribution of the chains [21]. For the sake of simplicity, we calculate the susceptibility of the disordered system, χ_{IJKL}, assuming that the distribution is uniform with respect to the angle ϑ in the interval from zero to an angle ϑ_0 and zero elsewhere, where the ϑ_0 describes the amount of disorder, ranging from 0 (completely ordered system) to $\pi/2$ (completely disordered system):

$$\mathrm{X}_{IJKL} = \frac{1}{2\pi\left(1-\cos\vartheta_0\right)}\int_{-\pi}^{\pi}d\varphi\int_{0}^{\vartheta_0}d\vartheta\sin\vartheta\, C_{Ii}C_{Jj}C_{Kk}C_{Ll}\chi_{ijkl}. \tag{4}$$

Integration over ψ is not needed since the system is already uniformly distributed around the z axis. It is worth noting that this angular averaging preserves the symmetry of the susceptibility around the Z axis. Therefore, X_{IJKL}, similarly to χ_{ijkl}, has only 21 non-zero terms with only three of them being independent:

$$\tilde{c}_{11} = c_{11} - q_1 t + \left(\frac{q_0}{2}+\frac{q_1}{3}\right)t^2 - \frac{3q_0}{8}t^3\left(1+\frac{t}{5}\right),$$

$$\tilde{c}_{16} = c_{16} + \frac{1}{2}\left(q_0+\frac{q_1}{3}\right)t - \frac{1}{6}\left(5q_0+\frac{q_1}{3}\right)t^2 + \frac{q_0}{2}t^3 - \frac{q_0}{10}t^4, \tag{5}$$

$$\tilde{c}_{33} = c_{33} - 2\left(q_0-q_1\right)t + 2\left(q_0-\frac{q_1}{3}\right)t^2 - q_0 t^3 + \frac{q_0}{5}t^4,$$

where $q_0 = c_{33}+c_{11}-6c_{16}$, $q_1 = c_{11}-3c_{16}$, and $t = 1-\cos\vartheta_0$. Quite obviously, the limit of perfectly ordered system, $t\rightarrow 0$, yields $\mathrm{X} = \chi$.

As shown in [16], in the case here of interest of linearly polarized, rotating pump-and-probe beam and circularly polarized Stokes beam, both propagating perpendicularly to the Z axis, the generated CARS signal contains a dc component (A_{dc}) a component ($A_{2\omega}$) oscillating at 2ω, and a component ($A_{4\omega}$) oscillating at 4ω:

$$A_{dc} = 3\tilde{c}_{11}^2 + 2\tilde{c}_{11}\tilde{c}_{16} + 14\tilde{c}_{16}^2 + 2\tilde{c}_{33}\tilde{c}_{16} + 3\tilde{c}_{33}^2,$$

$$A_{2\omega} = 4\left(\tilde{c}_{11}^2 - \tilde{c}_{33}^2\right), \tag{6}$$

$$A_{4\omega} = \tilde{c}_{11}^2 - 2\tilde{c}_{11}\tilde{c}_{16} - 6\tilde{c}_{16}^2 - 2\tilde{c}_{33}\tilde{c}_{16} + \tilde{c}_{33}^2.$$

A further component at 6ω would be present if a rotating linearly-polarized Stokes beam were used instead of a circularly polarized one, which would give access to a more detailed description of the orientation distribution function [21]. Here we are not interested anyway to provide such description, but rather we shall show that the first two components, A_{dc} and $A_{2\omega}$, are fully sufficient to characterize the myelin health status in the present demyelinating model. For this reason rotating also the Stokes beam (linear) polarization would be an unnecessary technical complication, as discussed in [16].

In the limit of perfectly ordered system, $t\rightarrow 0$, the equations above reduce to those reported in [16], while some algebraic manipulations confirm that for $t\rightarrow 1$, i. e. for a completely randomized system, $A_{2\omega} = A_{4\omega} = 0$. This behavior is shown in Fig. 2(a) that reports the inverse tangent of $A_{2\omega}/A_{dc}$ (top graph) and the values of A_{dc}, $A_{2\omega}$, and $A_{4\omega}$ as a function of t (bottom graph), calculated taking the values of the components of χ from [18]. The squared modulus of the third-order polarizability ($|\mathrm{P}|^2$) of the system when excited with

linearly polarized pump-and probe photons and circularly polarized Stokes photons as a function of the angle η between the polarization plane of the pump-and-probe beam and the *X-Y* plane is shown in Fig. 2(b). In particular, $|P|^2$ for a completely disordered system ($t = 1$) has no dependence on the pump-beam polarization orientation. Whereas $|P|^2$ in an ordered system ($t < 1$) is highest when the pump beam polarization orientation is parallel respect with the molecular-bond dipole and lowest when it is perpendicular to it, with the modulation amplitude increasing with decreasing *t*.
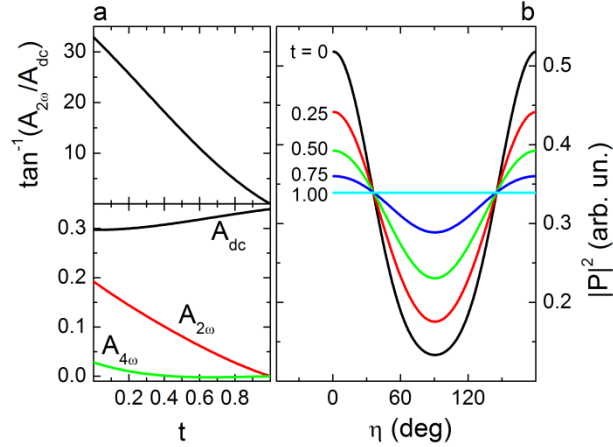

Fig. 2. (a) Top graph: inverse tangent of $A_{dc} / A_{2\omega}$ as a function of the disorder parameter *t*. Bottom graph: dc and ac amplitudes (in arbitrary units) of the squared modulus of the third-order polarizability ($|P|^2$) of the system when excited with linearly polarized pump-and probe photons and circularly polarized Stokes photons as a function of *t*. (b) $|P|^2$ at different values of the disorder parameter as a function of the angle η between the polarization plane of the pump-and-probe beam and the *X-Y* plane.

It is apparent from Fig. 2(a) that the disorder parameter *t* is closely related to the inverse tangent of $A_{2\omega} / A_{dc}$, which is a quantity – expressed in degrees in the figure – that can be directly measured with the RP-CARS setup:

$$\alpha = \tan^{-1}\left(\frac{A_{2\omega}}{A_{dc}}\right) \qquad (7)$$

We find particularly interesting here the possibility to quantify the amount of disorder with a ratiometric quantity in order to remove contributions from difficult-to-measure quantities, such as the laser power delivered to the sample, the collection efficiency of the optics, and the sensitivity of the PMTs. To this end it is very convenient to express the relation between A_{dc} and $A_{2\omega}$ as an angle (α) rather than, i. e., with their ratio, as the former is much less sensitive to noise with respect to the latter, especially in regions of the image where the density of CH_2 bonds is low (small A_{dc}).

4. Results and discussion

Here we shall show that the aforementioned spatial anisotropy of CH_2 bonds is a good indicator of myelin health or damage. In order to obtain controlled and measurable myelin damage we acutely exposed an explanted sciatic mouse nerve to lysophosphatidylcholine (lyso-PtdCho), a well-known demyelinating agent [7, 22].

Lyso-PtdCho exerts its action via a calcium dependent pathway [7] and induces a swelling and a disruption of the myelin architecture, from the outside to the inside of each fiber

(partially at the expense of the fiber lumen) as depicted in the inset of Fig. 3. It was early recognized, using transmission electronic microscopy [22], that the main effect of the lyso-PtdCho was to disorganize the juxtaposition of the concentric myelin layers, thereby making them less compact and less symmetrically ordered around the fiber main axis. However, the important role played in this process by the lytic enzymes calpains and phospholipase A_2 (PLA2) was recently acknowledged [7]. It is reasonable to assume that, during the lyso-PtdCho induced demyelinating process, the PLA2 hydrolyzes the myelin phospholipids into lysophospholipids and fatty acids. The increase in molecular spatial degrees of freedom caused by the PLA2-catalyzed cleavage of the second acyl bond in the glycerol moiety (or the removal of the fatty acid from the membrane) translates in our model simply into an increase of the *t* parameter. Quite likely, these are not the only biochemical processes occurring in this experimental model and therefore our theoretical model cannot be expected to yield quantitative results (also because the numerical values of the susceptibility-tensor elements are not universal and they might change during the process), yet it is tempting to quantify the amount of damage in the myelin layers with the parameter α. In order to compare it to a reference health indicator, we computed the g-ratio for each nerve fiber, at present the best image-based index of myelin damage known in literature [7, 23–25]. The g-ratio is defined as the ratio between the inner and the outer diameter of the myelinated fiber as depicted in the inset of Fig. 3b. The g-ratio for healthy myelin fiber is usually about 0.6-0.7. In our demyelination model the g-ratio decreases as a function of time as the damage progresses. Please note that other authors [7] report that the exposition to lysophosphatidylcholine induces an increase (rather than a decrease) of the g-ratio. This apparent discrepancy occurs because Cheng et al. [7] take into account only the undamaged myelin in the calculation of the g-ratio, while we include the entire myelin sheath, i. e. both the healthy and the swollen parts. We decided to compute the g-ratio in this way, even if higher g-ratio values are consistently associated with myelin damage in literature, because we observed that the myelin compact region completely disappears while the nervous fiber alteration process is manifestly still ongoing.
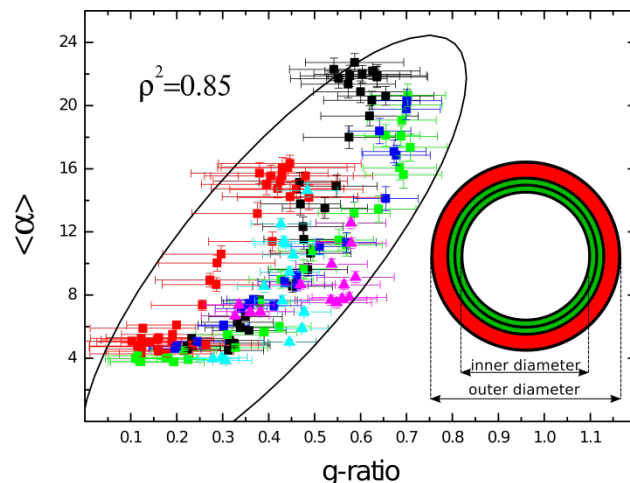

Fig. 3. Correlation plot between the g-ratio and the effective angle <α>. Different colors denote different nervous fiber, while different shapes (squares, triangles) denote experiments on different nerves (different mice). The ellipse describes the 95% confidence interval. The correlation coefficient (ρ^2) is 0.85 and the p-value is <0.001 (Spearman's rank correlation coefficient). Inset: In the lyso-PtdCho damage model the chemical demyelinating agent induces myelin damage (in red) and swelling from the outside to the inside of the fiber. The swelling induces both a reduction of the internal lumen and a growth of the global nerve fiber diameter. Therefore, since the inner diameter is reduced and the outer diameter is enlarged, the ratio between the two (g-ratio) is greatly reduced.

Since the g-ratio is a fiber-based indicator rather than a pixel-based one, as it is the angle alpha, we define an effective alpha, <α>, defined as:

$$< \alpha > = \tan^{-1} \left(\frac{\sum_i A_{2\omega,i}}{\sum_i A_{dc,i}} \right) \qquad (8)$$

Consistently with our theoretical model and with the observations reported in [7], <α> is found to decrease with time. Notably, we observe a remarkably good correlation (correlation coefficient: 0.85, p-value<0.001, Spearman's rank correlation coefficient) between the g-ratio values and <α>, as shown in Fig. 3. This demonstrates that our technique is well suited to visualize the alteration in myelin sheaths. Moreover, the computation of the g-ratio is a time-consuming task, as it requires to manually trace all the fibers, while our method is very fast, as it requires only to select the myelin wall region.

In the plot shown in Fig. 3, <α> saturates at approximately 4 degrees at low g-ratios corresponding to a $A_{2\omega}/A_{dc}$ ratio of about 7%. The same value is also found analyzing myelin-free image areas, such as the fiber lumen. However, if we compute <α> substituting the scalar sum at the numerator of Eq. (8) with a vector summation $\left| \sum_i \vec{A}_{2\omega,i} \right|$ (i.e. taking into account also the ψ value of each pixel and computing the magnitude of the resulting vector), the $A_{2\omega}/A_{dc}$ background value drops down to 3%. This value is consistent with the effect caused by the residual distortion of the polarizations presents in the incoming beams, as discussed in the 2.1 section. Using a scalar mean function is reasonable with sufficiently high $A_{2\omega}$ values but could lead to a slightly overestimation of α in regions of low $A_{2\omega}$, where a vector mean function is more appropriate, yet the latter would fail when computed over fibers that are curved in the imaging plane. Following these considerations, we estimate that other effects that could yield polarization distortions, such as myelin birefringence [26], are negligible in our experimental configuration, consistently with the fact that the imaging was not performed very deep within the nerve (< 40 μm) and that the signal was collected in the epi direction.

Since our algorithm is pixel based, we are also able to color-map the α value to create images in artificial colors (displayed in Fig. 4), yielding a real-time, pixel-by-pixel indication of the myelin health status during the acquisitions and to have a very intuitive representation of the on-going damage.
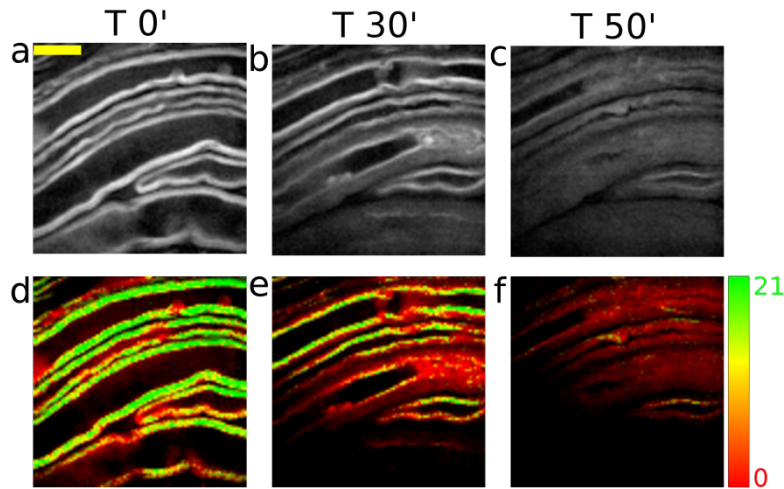
Fig. 4. Explanted sciatic nerve myelinated fibers imaged by RP-CARS. Top row (a, b, and c panels): grayscale images of the A_{dc} signal. Bottom row (d, e, and f panels): color maps of α. In the HSV color representation, the hue ranges from red to yellow to green at increasing values of α, as depicted in the color bar at the bottom-right, while the value is proportional to A_{dc} and the saturation is kept at maximum. Columns represent acquisitions after 0 minutes (first column), 30 minutes (second column) and 50 minutes (third column) from the initial exposure to the lyso-PtdCho. Scale bar: 10 μm.

The pixel-based α value ranges from a minimum of 0 in the ideal case to a sample-specific maximum (21 in this experiment). The sample-specificity of the maximum value is a consequence of the sample-related variability of the myelin composition and therefore of the value of the susceptibility tensor. However, as discussed before in this section, even though we have to take into account a sample-specific maximum value for α in order to perform comparative studies (similarly to what is commonly done with the g-ratio) the qualitative behavior of α as function the sample molecular disorder is not expected to change.

We note here that there are several factors that can factitiously reduce α: photomultiplier noise and CARS non-resonant background can increase the measured value of A_{dc} therefore leading to an underestimation of α. However this effect does not affect significantly the images being it relevant only in pixels associated with small A_{dc} and $A_{2\omega}$ values or, in other words areas that are colored in black. It should also be noted that the present method assumes that the symmetry axis of the acyl-chain distribution lies in the imaging plane within the point-spread function. An out-of-plane component of the axis leads to a reduction of the measured value of α. Indeed, in the extreme case when the symmetry axis is perpendicular to the imaging plane (e.g. when the imaging plane is tangent to the myelin wall), this method would erroneously yield α = 0. This is visible for example in the lower-left corner of Fig. 4d, where the imaging plane is almost tangent to the myelin sheath. Also myelinated fibers with a very small radius lead to a factitiously reduced angle. These cases are easily recognizable by eye and, therefore, excludable from the analysis.

5. Conclusions

RP-CARS is a novel microscopy technique derived from Coherent Anti-Stokes Raman Scattering. It exploits the well known polarization-dependent selection rules characteristic of CARS to efficiently detect the orientation and the anisotropy of selected molecular bonds in complex structures such as myelin. By correlating the measured anisotropy with the g-ratio,

we demonstrated here that our technique is well suited to visualize even the smallest alteration in myelin sheaths. The α value can be directly measured on a pixel-by-pixel basis and does not require three-dimensional acquisitions and complex post-acquisition analysis of the images. Therefore the approach presented here allows a direct color-coded visualization of the health status of myelinated fibers in real time. We believe that this method can significantly impact the experimental study of progressive demyelinating diseases, such as multiple sclerosis and leukodystrophies (i. e. Krabbe disease).